Taylor & Francis
Taylor & Francis Group

Validation of the MODIS active fire product over Southern Africa with ASTER data

JEFFREY T. MORISETTE*†, LOUIS GIGLIO†, IVAN CSISZAR‡ and
CHRISTOPHER O. JUSTICE‡

†NASA Goddard Space Flight Center, Greenbelt, MD 20771, USA
‡Department of Geography, University of Maryland, 2181 LeFrak Hall, College Park,
MD 20742, USA

This paper describes the use of high-spatial-resolution ASTER data to determine the accuracy of the moderate-resolution MODIS active fire product. Our main objective was to develop a methodology to use ASTER data for quantitative evaluation of the MODIS active fire product and to apply it to fires in southern Africa during the 2001 burning season. We utilize 18 ASTER scenes distributed throughout the Southern Africa region covering the time period 5 August 2001 to 6 October 2001. The MODIS fire product is characterized through the use of logistic regression models to establish a relationship between the binary MODIS 'fire'/'no fire' product and summary statistics derived from ASTER data over the coincident MODIS pixel. Probabilities of detection are determined as a function of the total number of ASTER fires and Moran's I, a measure of the spatial heterogeneity of fires within the MODIS pixel. The statistical analysis is done for versions 3 and 4 of the MODIS fire-detection algorithm. It is shown that the algorithm changes have a positive effect on the fire-product accuracy.

1. Introduction

The objective of the Southern Africa Fire and Atmosphere Research Initiative (SAFARI) is to investigate the Earth–atmosphere–human interaction through an extensive field campaign, including ground-, air- and space-based observations of various biogeophysical and biogeochemical processes (Swap *et al.* 1998). Among these processes is the emission of gases and particulate matter into the atmosphere by natural and agricultural biomass burning. A critical part in the process of understanding the influence of fire on the atmosphere is to have accurate and reliable information on the timing of fires and their location.

The most practical way of obtaining large-scale maps of fire occurrences is to use moderate- to high-resolution radiometers on board satellites (Justice and Korontzi 2001). For a long period, the Advanced Very High Resolution Radiometer (AVHRR) on board the polar orbiter NOAA satellites was the only instrument that provided observations of the spatial distribution of fire hot spots on a global scale with relatively high temporal frequency. Additional instruments on board other platforms began to be exploited for fire monitoring in the following decade, including the Geostationary Orbiting Environmental Satellite (GOES), Visible Infrared Spin Scan Radiometer Atmospheric Sounder (VAS) (Prins and Menzel

*Corresponding author. Email: jeff.morisette@nasa.gov

1992), the GOES Imager (Menzel and Prins 1996), the Defense Meteorological Satellite Program (DMSP), Operational Linescan System (OLS) (Elvidge and Baugh 1996), the Along Track Scanning Radiometer (ATSR) (Arino and Rosaz 1999), the Tropical Rainfall Measuring Mission (TRMM) and the Visible and Infrared Scanner (VIRS) (Giglio *et al.* 2000). However, these instruments' characteristics are not optimal for fire detection. Nevertheless, AVHRR data have been successfully used for mapping fires during the SAFARI 1992 campaign, using a multi-spectral and contextual algorithm appropriately tuned for local conditions (Justice *et al.* 1996).

The Moderate Resolution Imaging Spectroradiometer (MODIS; Kaufman *et al.* 1998) is a 36-band instrument with substantially improved capabilities for fire mapping as compared with the AVHRR. The first MODIS sensor is onboard the Terra satellite, which was launched in December of 1999 and has a daytime local overpass of about 10.30 a.m. The second MODIS sensor is onboard the Aqua satellite, launched in May 2002, with a 1.30 p.m. daytime overpass. One of the land products derived from the MODIS sensor is a pixel-resolution fire mask, separated into files representing 5 min of image acquisition along a given swath (Justice *et al.* 2002a). The increased saturation temperatures of the 1 km resolution 3.9 μm and 11 μm sensors decrease the ambiguities leading to false alarms or omission errors typical of the AVHRR-based fire products (Giglio *et al.* 2003). The first MODIS sensor is onboard the Terra satellite, launched in December of 1999, and has a daytime local overpass of about 10.30 a.m. The second MODIS sensor is onboard the Aqua satellite, launched in May 2002, and has a 1.30 p.m. daytime overpass. The main objective of this paper is to develop a methodology to use ASTER data for quantitative evaluation of the MODIS active fire product and to apply it to fires in Southern Africa during the 2001 burning season, concentrating only on imagery from the daytime overpass.

The Advanced Spaceborne Thermal Emission and Reflection Radiometer (ASTER) (Yamaguchi *et al.* 1998), also onboard the Terra satellite, provides near-nadir view measurements in four visible and near-infrared bands between 0.52 and 0.86 μm, six shortwave infrared (SWIR) bands between 1.6 and 2.43 μm, and five thermal infrared (TIR) bands between 8.125 and 11.65 μm at 15, 30 and 90 m resolutions, respectively. The coincident high-resolution, multi-spectral measurements within a $\sim$60 km swath near the centre of the MODIS swath provide a unique opportunity to analyse the fine-scale features within the MODIS pixels, such as active fires.

Figure 1 is an ASTER band 9 (2.4 μm) grey-scale image of a large fire complex in Namibia. Overlain are the MODIS 1 km footprints, with white boxes denoting pixels flagged as fires by the MODIS version 3 fire product. The superior representation of the fine-scale details of the fire by ASTER is obvious. Omission and commission errors from MODIS are also visible. For example, the MODIS algorithm failed to detect distinct fire fronts within pixels, particularly in the upper part of the image. Also, some pixels with no fire signal from ASTER were flagged by the MODIS algorithm as containing fire. These commission and omission errors underline the limitations of the MODIS fire algorithm and the need for quantification of its accuracy.

The input data for this study are presented in section 2. In section 3, a procedure to create binary ASTER fire masks within the MODIS footprints and a method for their statistical comparison with the MODIS product are described. Results of the analysis are presented in section 4 for both versions 3 and 4 of the MODIS
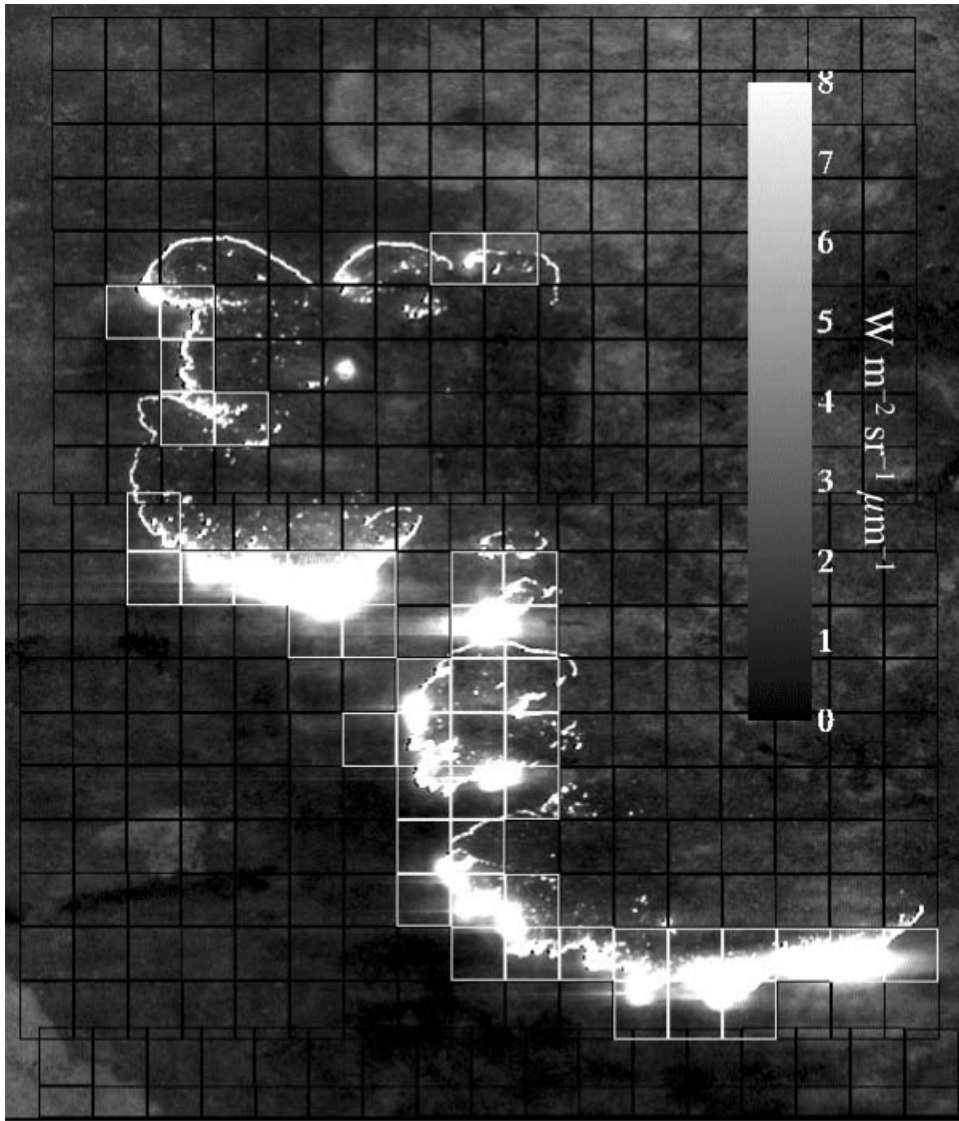
Figure 1. ASTER 2.4 μm (band 9) image of a large fire complex from 17 August 2001 9:08 UTC, centred at 18.8° S 19.9° E. The gridded overlay denotes the nominal footprints of the MODIS pixels. The white boxes represent MODIS-detected fire pixels from the version 3 algorithm.

fire-detection algorithm. The statistical analysis is followed by a discussion of the results in section 5.

2. Materials

2.1 *MODIS fire products*

Although 8-day composites of the MODIS fire products exist (Justice *et al.* 2002a), validation using temporally coincident observations (as in the present work) is most straightforward with the swath-based daily fire product, referred to as the MODIS

Level 2 product. This product, which is used to produce all higher-level fire products, is defined in the MODIS orbit/viewing geometry, and contains active fire information for a 5 min segment of the orbital swath. Specifically, the Level 2 fire product contains multiple image layers and an extensive table of information about individual fire pixels. Of relevance to this study is the active fire mask, in which fires and other pixel classes of interest, such as cloud, are identified.

In response to algorithm and instrument problems, successive versions of the Level 2 fire product have been generated since acquisition of MODIS data began in early 2000. We utilized the current Level 2 MODIS fire product, version 4, which is available from the Land Processes Distributed Active Archive Center (LP DAAC) (http://lpdaac.usgs.gov/), as well as the older version 3 MODIS fire product. The version 4 algorithm was developed in response to persistent problems that were observed in the version 3 product, including persistent false alarms in sparsely vegetated regions, and an inability to detect small yet obvious fires (Justice *et al.* 2002a, Giglio *et al.* 2003). Consideration of both versions provided a quantitative assessment of the improvements incorporated into the version 4 fire algorithm. The version 4 algorithm has been used for production since the inception of the 'Collection 4' reprocessing in late 2002, at which time improvements to sensor calibration and geolocation were also incorporated into the processing stream.

The MODIS Level 1A 1 km 5 min swath geolocation product, coincident with the MODIS Level 2 fire-product data, was used to obtain the location of individual pixels within the Level 2 fire product. The geolocation accuracy from the MODIS operational preprocessing is a fraction of a pixel (Wolfe *et al.* 2002) as compared with three or four pixels for the AVHRR.

2.2 *ASTER data*

In this paper, we derived high-resolution binary 'fire'/'no fire' maps from ASTER data for 18 ASTER scenes falling within 11 MODIS granules (table 1; Morisette *et al.* 2003). In addition to this dataset, several other representative cases were used for demonstration and statistical model evaluation purposes (such as that in figure 1). The data are spread across various ecosystems in the Southern African region from dry grassland in the Kalahari region to savannah towards the North (figure 2). All data are from the morning/daytime overpass of the Terra Satellite.

The ASTER scenes were version 2 'ASTER L1B registered radiance at the sensor' products acquired from LP-DAAC. The digital count values were converted into radiances using the unit conversion coefficients provided within the L1B files. Since this analysis, version 3 of the same product has also become available. However, a comparison of sample version 2 and version 3 data revealed no differences in the information extracted from that imagery for this study. Therefore, we deemed that repeating the analysis with version 3 ASTER data was unnecessary.

3.   Methods

3.1   *Independently derived ASTER high-resolution fire maps*

3.1.1   ASTER band selection. ASTER does not have a band corresponding to the MODIS 3.9 μm 'fire' bands, which are highly sensitive to thermal emissions at usual fire temperatures. However, with the high spatial resolution of the ASTER sensor, even a relatively small fire can cover a considerable fraction of the ASTER pixel. With this, the relative contribution of the increased thermal emission from fires, as

Table 1. Parameters of the ASTER and MODIS files used to derive the statistical models of MODIS fire-detection probability.

Scene	ASTER filename	Date	Latitude (°)	Longitude (°)	Coincident MODIS granule ID
1	pg-PR1B0000-2001081702_091_001	5 August	−14.04	27.53	MODxx.A2001217.0840.vvv.*.hdf
2	pg-PR1B0000-2001081702_095_001	5 August	−19.39	26.36	MODxx.A2001217.0840.vvv.*.hdf
3	pg-PR1B0000-2001091402_112_001	1 September	−12.69	30.48	MODxx.A2001244.0820.vvv.*.hdf
4	pg-PR1B0000-2001091402_031_001	1 September	−16.96	29.52	MODxx.A2001244.0820.vvv.*.hdf
5	pg-PR1B0000-2001091602_042_001	4 September	−12.98	24.73	MODxx.A2001247.0850.vvv.*.hdf
6	pg-PR1B0000-2001091602_045_001	4 September	−15.65	24.15	MODxx.A2001247.0850.vvv.*.hdf
7	pg-PR1B0000-2001092202_069_001	9 September	−14.98	18.69	MODxx.A2001252.0910.vvv.*.hdf
8	pg-PR1B0000-2001092202_001_001	9 September	−22.46	16.98	MODxx.A2001252.0910.vvv.*.hdf
9	pg-PR1B0000-2001100702_081_001	18 September	−18.19	44.26	MODxx.A2001261.0725.vvv.*.hdf
10	pg-PR1B0000-2001101102_017_001	23 September	−12.33	16.31	MODxx.A2001266.0920.vvv.*.hdf
11	pg-PR1B0000-2001101302_111_001	28 September	−17.17	35.56	MODxx.A2001271.0800.vvv.*.hdf
12	pg-PR1B0000-2001101302_275_001	28 September	−13.96	36.26	MODxx.A2001271.0800.vvv.*.hdf
13	pg-PR1B0000-2001101502_039_001	29 September	−13.24	24.27	MODxx.A2001272.0845.vvv.*.hdf
14	pg-PR1B0000-2001101502_050_001	29 September	−22.31	22.15	MODxx.A2001272.0845.vvv.*.hdf
15	pg-PR1B0000-2001101603_130_001	1 October	−11.29	29.14	MODxx.A2001274.0830.vvv.*.hdf
16	pg-PR1B0000-2001101603_155_001	2 October	−12.32	17.78	MODxx.A2001275.0915.vvv.*.hdf
17	pg-PR1B0000-2001101603_017_001	2 October	−13.92	17.43	MODxx.A2001275.0915.vvv.*.hdf
18	pg-PR1B0000-2001102002_118_001	5 October	−26.83	32.13	MODxx.A2001278.0810.vvv.*.hdf

Multiple MODIS files were used. The table lists the common elements for all MODIS filenames. In the actual filenames, 'xx' is either 03 for geolocation files or 14 for fire products files, 'vvv' is the version number (003 for MOD03, 003 and 004 for MOD14), and '*' is the processing date and time.
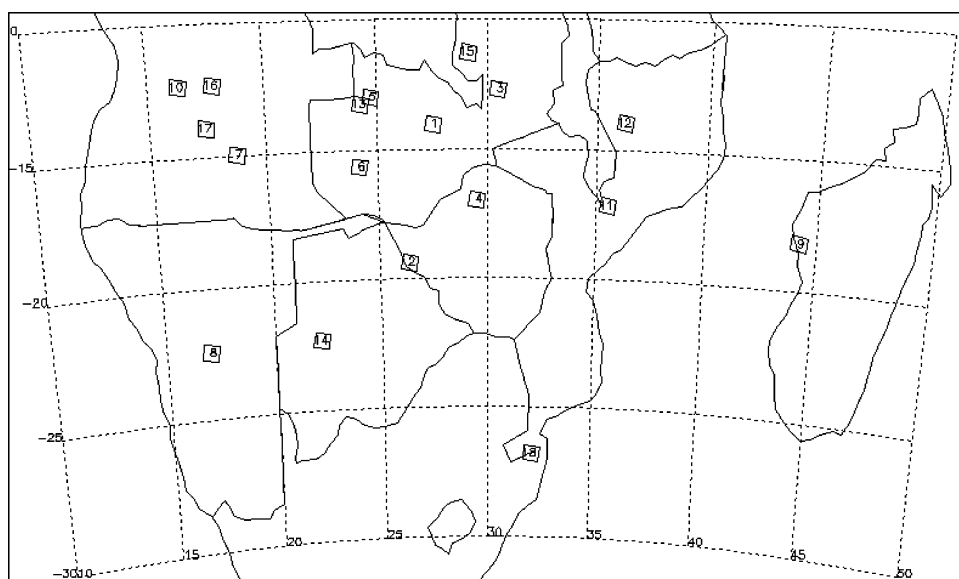
Figure 2.	Spatial coverage of the ASTER scenes used to derive the statistical models of MODIS fire-detection probability. The numbers indicate the file numbers in table 1.

compared with the background, is substantial enough to produce a distinct fire signal in both the SWIR and TIR bands.

The SWIR subsystem of ASTER has four gains: high, normal, low-1 and low-2. All the scenes used in this study have SWIR data acquired at normal gain, which is the default operating mode. At normal gain, high-temperature targets often cause the digital count from the sensor to reach the saturation value of 255 (Justice *et al.* 2002a), corresponding to brightness temperatures of 892 K at band 4 (1.65 μm), 695 K at band 5 (2.17 μm), 681 K at band 6 (2.21 μm), 681 K at band 7 (2.26 μm), 636 K at band 8 (2.33 μm) and 610 K at band 9 (2.40 μm). However, in the SWIR region, the integrated radiance detected by the sensor is the sum of reflected solar radiation and emitted thermal radiation. According to theory, the relative contribution of the reflected solar radiation in the SWIR region decreases with increasing wavelength. Thus, band 9, even though it saturates at a lower temperature, allows the best separation between fires and any background signals among the ASTER SWIR bands.

In the TIR region, which lacks appreciable reflected solar radiation, the success of detecting fire hotspots depends on the relative contribution of emitted radiance from the fire to the integrated emitted signal, including the fire-free background. In the coarser-resolution TIR bands, however, the fractional fire area is smaller than in the SWIR bands. According to Planck's law, at typical fire temperatures, the relative sensitivity of radiance to temperature decreases with increasing wavelength, suggesting the use of the TIR bands with the shortest wavelength. Note that the ASTER TIR bands have only gains with a ~370 K saturation brightness temperature.

Figure 3 shows ASTER band 9 (2.4 μm) and 10 (8.3 μm) images of part of the fire complex shown in figure 1. Both grey-scale images are stretched in a similar fashion from 0 to the saturation radiance value. Comparing the two images indicates that band 9 distinguishes many more details of the fire front and detects smaller,
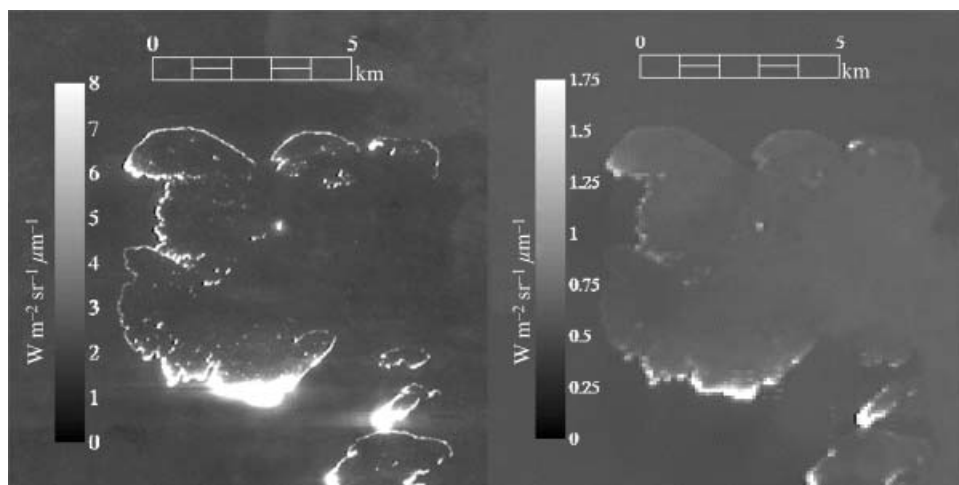
Figure 3.   ASTER 2.4 μm (band 9 (*a*)) and 8.3 μm (band 10 (*b*)) images of a fire.

individual fires as well (note also the increased thermal signal in band 10 from the recently burned areas). Based on theoretical considerations and multiple visual comparisons, we decided to use only band 9 for the identification of active fires from ASTER data.

3.1.2 Fire identification. Scrutiny of a number of ASTER band 9 images established that the vast majority of obvious fire pixels have a radiance at or near the saturation value of $8.04 \, \mathrm{W \, m^{-2} \, sr^{-1} \, \mu m^{-1}}$. However, bright clouds, bright or hot land surfaces, and sun-glint can be mistaken as fires unless a careful analysis of the data is done. Because of this, each of the individual ASTER scenes was visually inspected. Sun-glint was found to be absent from all the ASTER scenes used in this study because of the sun-surface-sensor geometry for our particular area and period of interest.

Typical ASTER band 9 radiance values for clear surface, clouds, and fires are illustrated in figure 4. The image on the left shows a highly reflective cloud near a fire cluster. The histogram of the same image reveals two distinct humps, representing cloud-free background land surface and the cloud. The flat part of the histogram above $6.33 \, \mathrm{W \, m^{-2} \, sr^{-1} \, \mu m^{-1}}$ corresponds to bright cloudy pixels (shown in red in the centre of the cloud in figure 4) and the non-saturated pixels in the fire fronts at the bottom. A spike of the histogram at the radiance value of $8.04 \, \mathrm{W \, m^{-2} \, sr^{-1} \, \mu m^{-1}}$ is also visible. From the histogram, it can be seen that the radiances corresponding to clear land surface remain under $\sim 4 \, \mathrm{W \, m^{-2} \, sr^{-1} \, \mu m^{-1}}$, and that most cloudy pixels remain under $\sim 6 \, \mathrm{W \, m^{-2} \, sr^{-1} \, \mu m^{-1}}$. However, it is obvious that there is some ambiguity between ~ 6 and $\sim 8 \, \mathrm{W \, m^{-2} \, sr^{-1} \, \mu m^{-1}}$ in terms of separating fire and bright cloudy pixels. Similarly, a few pixels clearly corresponding to the fire fronts have radiance values slightly under $6.33 \, \mathrm{W \, m^{-2} \, sr^{-1} \, \mu m^{-1}}$, associated with small fire fraction and/or lower temperatures from smouldering. Overall, the radiance value of $6.33 \, \mathrm{W \, m^{-2} \, sr^{-1} \, \mu m^{-1}}$ (or digital count value of 200 for ASTER's normal, default gain settings) is a reasonable compromise for the lower threshold for fire identification from ASTER band 9. While there is an obvious need for the development of an automated ASTER fire detection algorithm—including cloud screening—for this study we used this simple empirical
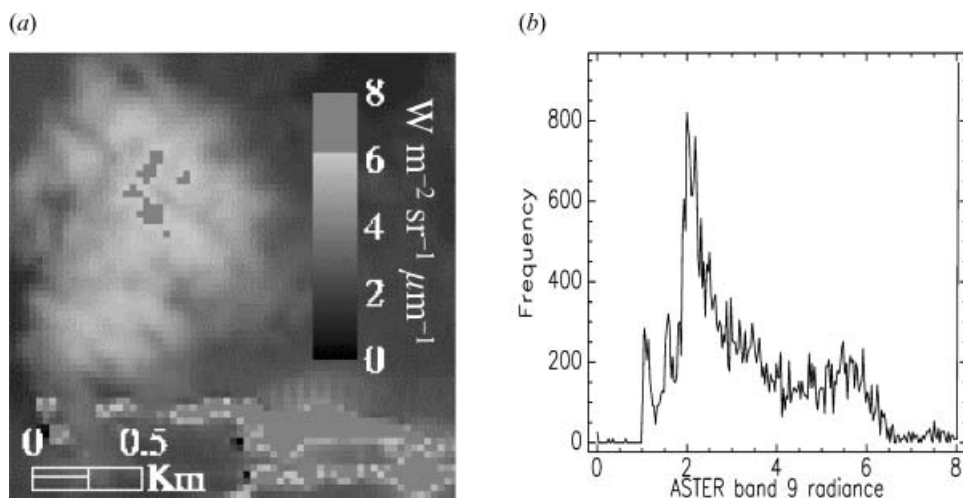
Figure 4. (*a*) Bright cloud in the vicinity of fires on an ASTER band 9 image taken on 1 October 2001 at 8:30 UTC, centred at 11.3° S and 29.1° E. The red overlay represents pixels with band 9 radiance value above 6.33 W m^{-2} sr^{-1} μm^{-1}. (*b*) Histogram of the band 9 radiances from the same image.

threshold to identify fires and then interactively eliminated any possible false signals. The semi-automated procedure, coupled with visual inspection, ensured that the derived binary ASTER fire product had the highest accuracy possible, given the available information.

In addition to the potential false fire alarms discussed above, ASTER band 9 data have also been found to exhibit three instrument-related artefacts that occur when a strong impulse of radiation reaches the sensor: (1) the bright target is surrounded by a circular 'bloom' of increased radiance values; (2) there is a distinct 'spike' of increased radiance values in the cross-track direction originating from the bright target; and (3) there are pixels with near-zero values at the edge or within the cluster of saturated pixels. The artefacts listed can be seen in figure 1. The near-zero radiances appear mostly to the left of fire fronts. The spikes and the blooms around more intense parts of the complex are also clearly visible. Fortunately, the radiance values within these areas are below ~6 W m^{-2} sr^{-1} μm^{-1}, and so they do not affect our analysis. However, they would need to be considered in studies where the quantitative characterization of pixels neighbouring the fire cluster is needed.

3.1.3 Creation of coincident ASTER binary fire masks. The procedure described above yields binary ASTER fire masks with a 30 m spatial resolution. To compare these with the 1 km MODIS fire masks, each ASTER pixel must be assigned to those MODIS pixels in which they fall. This mapping of ASTER pixels to MODIS pixels was performed using a nearest-neighbour search through all MODIS pixels overlapping the region viewed within the particular ASTER scene. An example of the result of this mapping procedure is shown in figure 1. Notable on that figure is the slight horizontal shift and vertical overlap of the MODIS pixel pattern towards the middle of the image, associated with the separate MODIS scans each producing 10 separate scan lines from 10 separate detectors.

Because of the along-scan triangular MODIS response at the surface (Kaufman *et al.* 1998), there is a 50% along-scan overlap in the area observed by two adjacent

MODIS 1 km pixel and overlap from triangular response
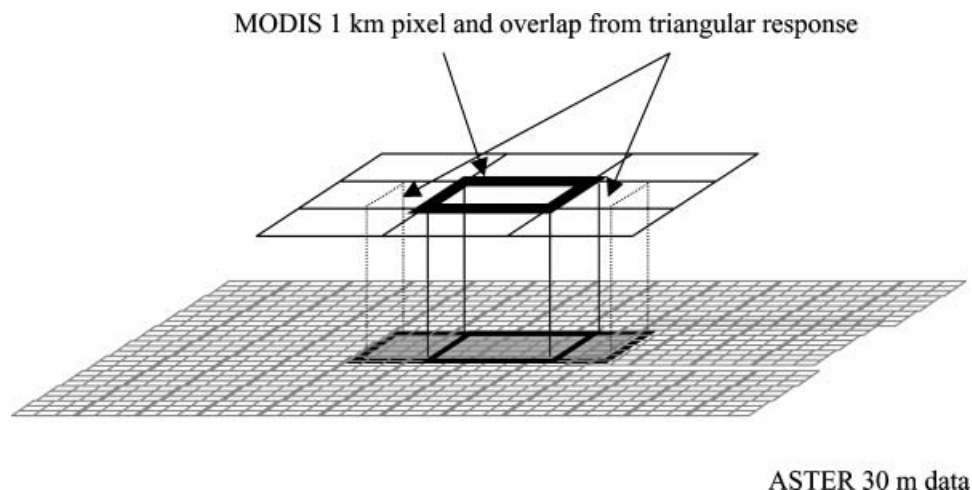

ASTER 30 m data

Figure 5. Diagram representing the ASTER fire map area summarized for each MODIS pixel, taking into account the triangular response function of the MODIS sensor.

MODIS pixels. Consequently, a single ASTER pixel will fall within two MODIS pixels, and a single fire can be detected twice. To account for the triangular response effect in the statistical analysis, MODIS pixels were considered to be 2 km in the along-scan direction and 1 km in the along-track directions (see figure 5). These dimensions describe near-nadir MODIS pixels only, but are appropriate for ASTER-based validation, since the ASTER pointing range is restricted to this region. Using this 'footprint', individual ASTER fire sub-scenes were extracted for each MODIS pixel.

The triangular response has implications for any validation study. Specifically, fires near the along-scan edges of the 2-km-wide MODIS pixels will generally remain undetected—through no fault of the detection algorithm—since their radiance will be weighted very weakly. (Because of the 1 km overlap between MODIS pixels, a fire in this region is likely to be detected, however, in the along-scan neighbouring pixel which will have the same fire located near its centre.) One could compensate for this instrument-induced artefact by weighting ASTER fire pixels based on their location within the corresponding MODIS pixel, i.e. interpolate between a unit response at the centre of the MODIS pixel and zero response at each along-scan edge. Since, ultimately, we require validation of the fire *product*, the quality of which is determined by the performance of both the *detection algorithm and the instrument*, we have counted all ASTER fire pixels equally and not attempted to 'factor out' the along-scan spatial response.

3.2 *Summarizing ASTER data relative to MODIS pixels*

Within a given MODIS pixel, there are many ways to summarize the corresponding ASTER fire map. We were most interested in summaries related to the spatial extent and distribution of fires. To get an idea of the spatial extent of fires, we simply sum the number of ASTER fire pixels. To capture a one-number summary of the spatial distribution of the fires, we calculated Moran's I from the ASTER fire map for the area representing each MODIS pixel. Moran's I is used to detect spatial patterns and testing for spatial autocorrelation (Haining 1990, section 6.2). In that Moran's I

can be used to detect spatial autocorrelation, we felt it would serve as a useful summary statistic that could be associated with each MODIS pixel to relay information about the spatial distribution of the fires. Moran's *I* function applied to the ASTER fire map for each MODIS pixel is:

$$\text{Moran's } I = n \frac{\sum_{i=1}^{n} \sum_{j=1}^{n} w_{i,j}(y_i - \mu)(y_j - \mu)}{\left(\sum_{i=1}^{n}(y_i - \mu)^2\right)\left(\sum_{i \neq j}\sum w_{ij}\right)}, \quad (1)$$

where *n* is the number of ASTER pixels covered by a MODIS pixel after accounting for triangular response; *i* and *j* index the ASTER pixels within the MODIS pixel; y_i represents the ASTER pixel's value (either 0 or 1); w_{ij} is 1 for the eight pixels, y_j, that are adjacent to pixel y_j and 0 for all others; and μ is the mean of the ASTER fire map for the area represented by the MODIS pixel. Moran's *I* statistic summarizes spatial correlation where values increasing from zero to one indicate an increasing spatial correlation (adjacent pixels are more likely to be the same value). Theoretically, values decreasing from zero indicate negative spatial correlation (adjacent pixels are more likely to be different values). In practice, for the data analysed here, all Moran's *I* values are greater than or equal to zero, where Moran's *I* equal to zero represents a MODIS pixel area in which all ASTER pixels were zero. Summary statistics similar to Moran's *I* include Geary's *C* as well as general cross-product statistics (Haining 1990, section 6.2). These all relay similar information. To keep the analysis as concise as possible, we consider only Moran's *I*.

While Moran's *I* was developed as a way to test the hypothesis of spatial auto-correlation (Haining 1990), here it is used simply as a quantitative formula to summarize 'clumping' of the ASTER fire pixels. The higher Moran's *I*, the more contiguous, or 'clumped', the ASTER fire pixels. Figure 6 demonstrates how Moran's *I* provides a one-number summary on the spatial distribution of fire. The figure shows the ASTER fire maps corresponding to two MODIS pixels. Both areas have 34 ASTER pixels classified as 'fire'. However, the image on the left shows that all the 34 fire pixels are contiguous, whereas the image on the right shows the 34 fire pixels to be fairly well distributed throughout the MODIS pixel. This is relayed through Moran's *I*, which, for the image on the left, is nearly twice as much as the image on the right.

In summary, for each MODIS pixel, we have the following: MODIS fire value of either zero or one, the number of ASTER fire pixels, and an index of the spatial distribution of the ASTER fires via Moran's *I*.
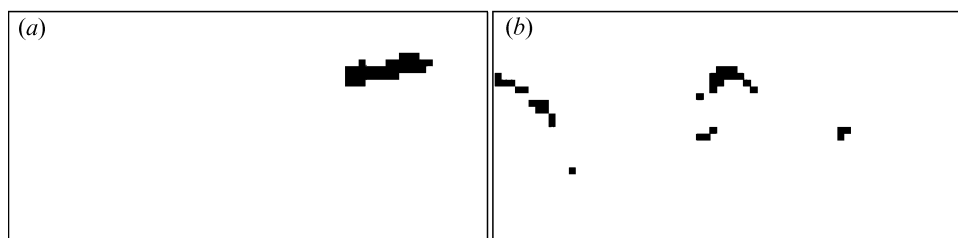
Total number of ASTER fire pixels = 34

Figure 6. Spatial distribution of ASTER fire pixels within MODIS footprints. (*a*) Moran's *I* = 0.681, variance = 0.0141; (*b*) Moran's *I* = 0.347, variance = 0.0139.

3.3 *Statistical method for comparison*

The comparison between MODIS and ASTER fire products addresses three major questions:

1. What are the characteristics of fires that MODIS will almost always detect (probability of detection > 0.95)?
2. What are the characteristics of fires that MODIS might detect (probability of detection $= 0.50$)?
3. What are the characteristics of fires that MODIS will likely miss (probability of detection < 0.05)?

In order to address these questions in a quantitative manner, we employ statistical models to relate the binary MODIS 'fire'/'no-fire' product with summary statistics from the ASTER fire map. MODIS data are taken to be the response (or 'Y') variable and the summary statistics derived from the ASTER data as the independent (or 'X') variable(s) within the context of logistic regression models. We consider two models. The first model includes only the ASTER fire counts as an explanatory variable:

$$\pi(x_i) = \frac{e^{\beta_0 + \beta_1 x_i}}{1 + e^{\beta_0 + \beta_1 x_i}}, \tag{2}$$

where x_i represents the count of ASTER fire pixels within MODIS pixel i, $\pi(x_i)$ is the probability that MODIS pixel i will be equal to 1 (i.e. labelled as 'fire') given the values of x_i, and the β_0 and β_1 parameters are estimated from the data (Agresti 1990).

The second model includes also Moran's I statistic as an explanatory variable:

$$\pi(x_i, m_i) = \frac{e^{\beta_0 + \beta_1 x_i + \beta_2 m_i}}{1 + e^{\beta_0 + \beta_1 x_i + \beta_2 m_i}}, \tag{3}$$

where, in the additional term, m_i represents Moran's I value for the ASTER fire pixels within MODIS pixel i, and now three terms: β_0, β_1 and β_2 are estimated from the data. Significant differences between models 1 and 2 will indicate the significance of including a measure of spatial continuity (i.e. Moran's I). More specifically, the significance of the β_2 parameter indicates the importance of including Moran's I in the model.

In order to account for the variability observed between ASTER scenes, models 1 and 2 are further refined to separate the within-scene variability from the between-scene variability. This is done using a mixed effect model (Pinheiro 2000) where scene differences are treated as a 'random effect' associated with experimental units, here the ASTER scenes. The mixed-effect versions of models 1 and 2 are:

$$\pi(x_{ij}) = \frac{e^{(\beta_0 + b_{0j}) + (\beta_1 + b_{1j})x_{ij}}}{1 + e^{(\beta_0 + b_{0j}) + (\beta_1 + b_{1j})x_{ij}}} \tag{4}$$

$$\pi(x_{ij}, m_{ij}) = \frac{e^{(\beta_0 + b_{0j}) + (\beta_1 + b_{1j})x_{ij} + (\beta_2 + b_{2j})m_{ij}}}{1 + e^{(\beta_0 + b_{0j}) + (\beta_1 + b_{1j})x_{ij} + (\beta_2 + b_{2j})m_{ij}}}. \tag{5}$$

As opposed to the fixed-effect parameters, the β_is, which are associated with the population, the random-effects parameters, the b_is, are instead associated with

experimental units drawn at random from the population. Although the random effects, the b_is, may behave like parameters, formally they are just another level of random variation, and random-effects modelling is used to separate (and estimate) a between-scene variability and within-scene variability (Pinheiro and Bates 2000).

The ASTER scenes used in this study were not selected with a true random sample, they were selected arbitrarily from a list of ASTER scenes that covered the area during the dry season. Thus, it seems appropriate to use the random effects model to account for between-scene variation. Including the differences between ASTER scenes as a random effect allows the model to incorporate the between-scene differences without limiting the resulting model to explicitly include the ASTER scenes identification. This allows the modelling to account for the difference between the scenes in an attempt to obtain a more accurate estimate of the 'fixed effects', or population parameters, the β_is. The resulting population model is equivalent in form to equations (2) and (3), but the β_is are fitted with models from equations (4) and (5), respectively.

The modelling is done with S-plus™ statistical software (Insightful Corporation, Seattle, WA). The resulting models are then used to address the three questions listed at the beginning of this section. We address the first question by evaluating the model at the $\pi(x_i)=0.05$ level, the second by considering $\pi(x_i)=.5$, and the third by evaluating the models at $\pi(x_i)=0.95$. While these particular values for $\pi(x_i)$ are somewhat arbitrary, the 0.05 and 0.95 values match probability levels typically associated with statistical testing, while values associated with the second question
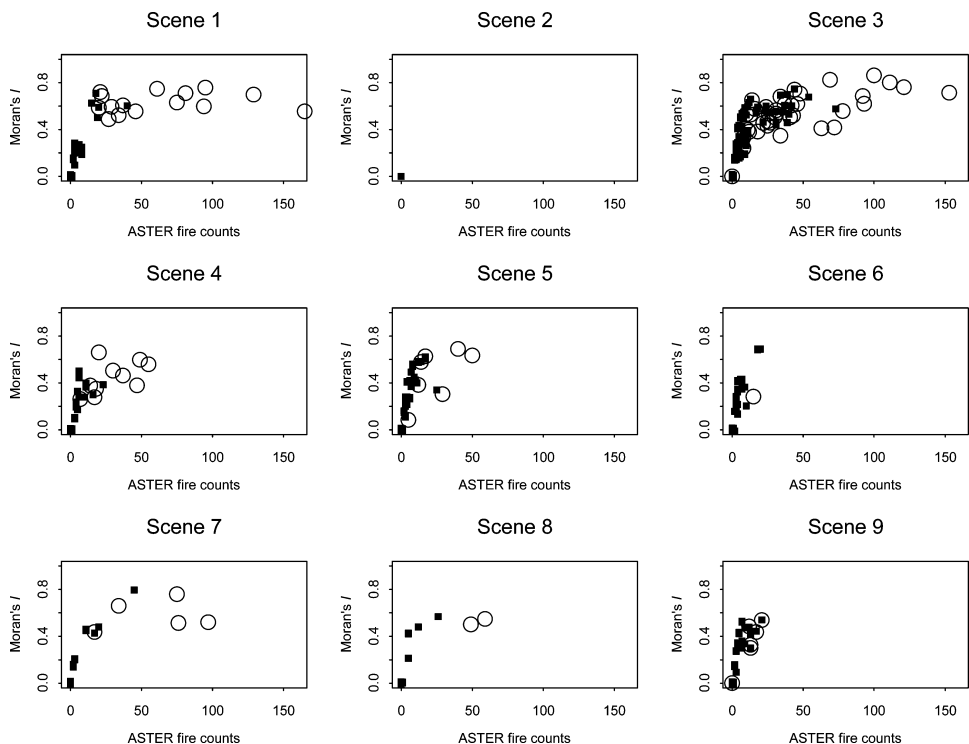

Figure 7. Scatter plot of ASTER fire counts and Moran's *I*. ○: MODIS fire pixels; ■: MODIS non-fire pixels.

correspond to the mid-point where the probability of detection is as likely as non-detection. Additionally, the actual models are given so that other values for $\pi(x_i)$ can be explored.

A standard method for assessing the accuracy of remotely sensed data is through the use of an error matrix. In the error matrix, the columns represent the reference data, while the rows represent the classified data (Aronoff 1982a, b). In this context, the ASTER imagery is the reference data, and the MODIS fire product is the classified data. However, for such an analysis, the reference data should be collected at the same minimum mapping unit as the map being assessed (Congalton and Green 1999). The error matrix approach requires using the same classification scheme for both the reference data and classified map. These two issues imply that we would need to consider all the ASTER data contained within a MODIS pixel and reduce it to a binary classification of either fire or non-fire. This, in turn, would require developing a method for such a classification, such as selecting a threshold for the number of ASTER fire counts beyond which we would classify the ASTER data within the MODIS pixel as 'fire'. Such a classification would involve a subjective selection of a threshold value and result in a serious reduction of the amount of ASTER information available within each MODIS pixel. With this, we utilize generalized linear modelling instead of the error matrix approach (Morisette and Khorram 2000).
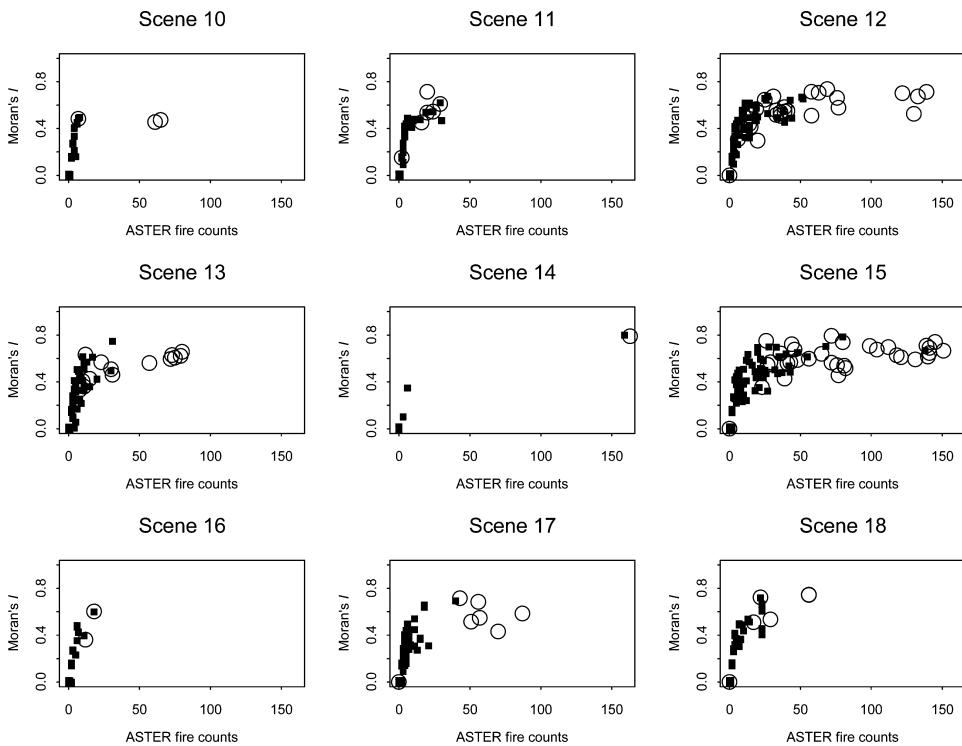

Figure 7.   (Continued).

4. Results

ASTER fire counts and Moran's *I* values for each MODIS pixel broken down scene by scene are shown in figure 7. It is worth noting that the majority of the data are from areas with no fire. That is, the closed squares at ASTER fire counts=0 and Moran's *I*=0 represent many pixels. However, as the data points are legitimate observations (Tappin 1994) representing the relationship between the MODIS and ASTER data, initially all data points are included in the model.

   The plots reveal several features of the data. First, the MODIS fire pixels tend to fall in the region with high ASTER fire counts and high Moran's *I* values. We also see several points where a fire pixel and a non-fire pixel overlap (a square within a circle). These represent areas where the fire fell near an along-scan edge of the MODIS pixel, thus falling in the region observed by two adjacent MODIS pixels due to the along-scan triangular response (see section 3.2). There is considerable variability between scenes, with one scene having no MODIS fire pixels (scene 2) and another containing 43 MODIS fire pixels. The sizes of fires within a scene also vary. For example, scene 6 has only one MODIS fire pixel, and the ASTER fire counts for that pixel are 15 while several pixels in scene 12 and 15 have ASTER fire counts above 200. This between-scene variability indicates that the data set captures much of the natural variability. It also indicates the need to utilize the random-effects models.

   To make general statements about the MODIS product, we move directly to results from analysis on the combined data from all scenes. This represents 66 761 MODIS pixels, of which 221 were flagged as 'fire' by the MODIS version 4 code.
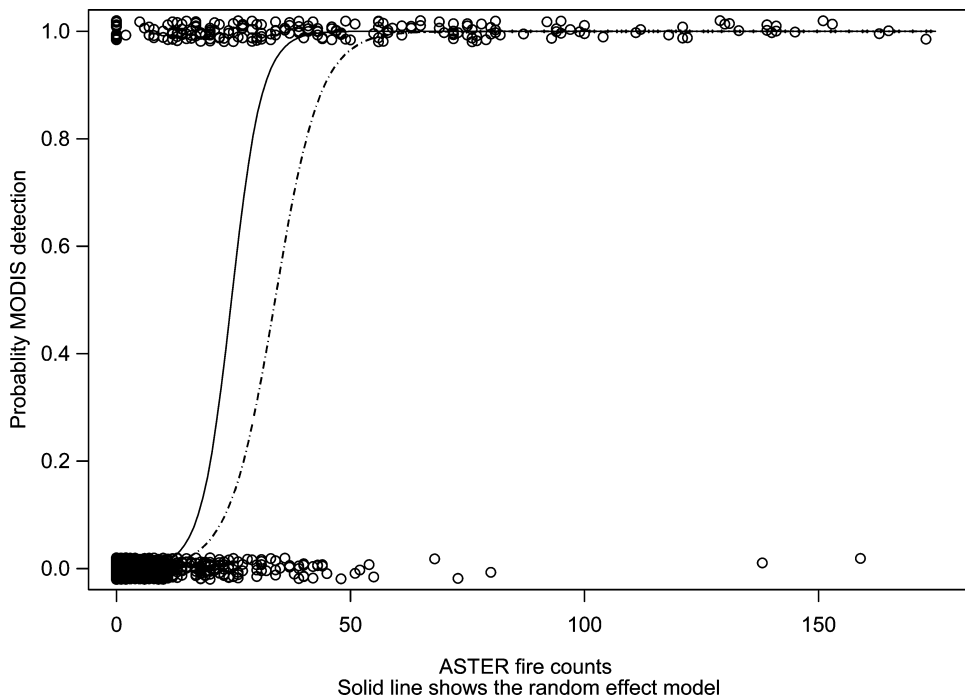

Figure 8.   Estimated probabilities from model 1, using the MODIS version 4 algorithm.

Table 2. Estimated model parameters from the various models.

				Residual deviance	Degrees of freedom
Algorithm: Version 3	$\beta_0,$	β_1			
Model 1	−7.305	0.154		873	66 759
Model 1 with random effects	−7.305	0.154		873	66 758
Algorithm: Version 4	$\beta_0,$	β_1			
Model 1	−7.006	0.207		1131	66 759
Model 1 with random effects	−7.577	0.308		884	66 758
Algorithm: Version 3	$\beta_0,$	β_1	β_2		
Model 2	−8.196	0.048	9.818	665	66 758
Model 2 with random effects	−8.221	0.054	9.320	635	66 757
Algorithm: Version 4	$\beta_0,$	β_1	β_2		
Model 2	−7.687	0.064	9.760	907	66 758
Model 2 with random effects	−7.762	0.113	8.528	821	66 757
Excluding data where ASTER fire counts=0					
Algorithm: Version 3	$\beta_0,$	β_1			
Model 1	−3.554	0.070		486	1078
Model 1 with random effects	−3.588	0.071		469	1077
Algorithm: Version 4	$\beta_0,$	β_1			
Model 1	−3.330	0.094		568	1078
Model 1 with random effects	−3.828	0.137		478	1077
Algorithm: Version 3	$\beta_0,$	β_1	β_2		
Model 2	−4.901	0.052	3.787	440	1077
Model 2 with random effects	−4.833	0.060	3.061	414	1076
Algorithm: Version 4	$\beta_0,$	β_1	β_2		
Model 2	−4.879	0.049	3.939	465	1077
Model 2 with random effects	−4.481	0.109	2.502	484	1076

Starting with model 1, we plot the data and the modelled relationship on figure 8. (Note, for the plot, a small random error has been added to MODIS values so as to better display overlapping points. The x axis is scaled to highlight the interesting portion of the model, and some points with higher ASTER fire counts and MODIS values of one are not shown on the graph.) The estimated parameters for the model are given in table 2, which also lists the residual deviance and degrees of freedom (Insightful 1999). The random-effects model parameters are given in table 2 and shown as the solid line in figure 8.

Table 3. ASTER fire count cut-off levels corresponding to probability levels at which MODIS will classify a pixel as 'fire' based on model 1.

	Probablity level				
Model	0.05	0.25	0.5	0.75	0.95
Version 3 algorithm					
No random effects	39.20	44.41	47.51	50.62	55.83
With mixed effects	39.20	44.41	47.51	50.62	55.83
Version 4 algorithm					
No random effects	27.70	31.58	33.89	36.20	40.07
With mixed effects	20.44	23.04	24.59	26.14	28.74

From the models, we can assign probability levels where the MODIS product will classify the pixel as fire for a given number of ASTER fire counts (table 3). For example, using the mixed-effects model, there is a 5% chance MODIS will classify a pixel as fire when the ASTER fire counts are roughly 20 pixels. Alternatively, there is a 95% chance MODIS will classify a pixel as fire when the ASTER fire counts within the MODIS pixel are over 30.

Points in the lower right of figure 8 represent ommision errors where a given point corresponds to many ASTER pixels classified as fire, yet the MODIS pixel was not classified as fire. Points in the upper left represent commission errors where a given point corresponds to few or no ASTER pixels classified as fire, yet the MODIS pixel was classified as fire. One could construct an error matrix (Aronoff 1982a, b, Congalton and Green 1999) by selecting a threshold along the 'ASTER fire counts' axis to divide the data into four groups of a 2×2 error matrix: MODIS=0 (no fire) and ASTER fire counts *below* the threshold, MODIS=0 and ASTER fire counts *above* the threshold, and two similar groups for MODIS=1 (fire). However, as mentioned earlier, the selection of the threshold is somewhat arbitrary and results in a reduction of data. The point is mentioned here only to aid our interpretation of figure 8.

The same modelling was applied to the MODIS version 3 algorithm results (figure 9). The mixed-effects models for the MODIS version 3 data yielded no practical difference—they are so close that neither line is discernible on figure 9, and the β_I parameters are identical to three decimal places. This is mainly due to the fact that for the version 3 data, the *within-scene* variability is large enough to make the *between-scene* variability relatively insignificant. The resulting model parameters are listed in table 2. Table 3 lists ASTER fire counts and corresponding probabilities for the version 3 algorithm.

Both the fixed- and random-effects models show that the version 4 algorithm has a better likelihood of detecting small fires. For a given probability of MODIS fire
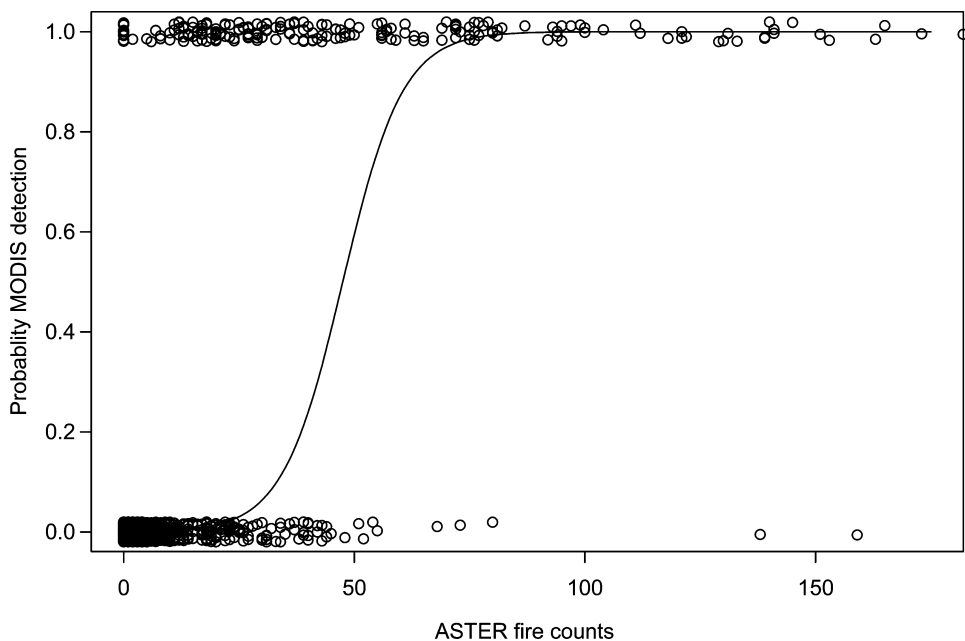

Figure 9.   Estimated probabilities from model 1, using the MODIS version 3 algorithm.
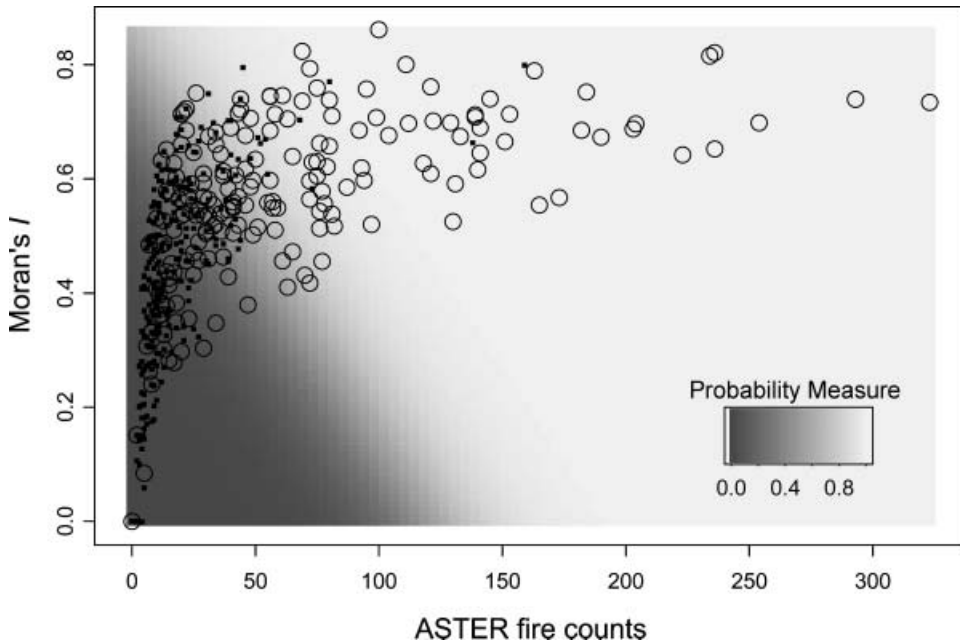
Figure 10. Estimated probabilities from model 2 using the MODIS version 4 algorithm.

detection, the number of ASTER fire pixels is lower for the version 4 data. Also, the fitted curves are steeper for the version 4 data, thus indicating a quicker transition between the number of ASTER fire counts where MODIS is unlikely to classify the data as non-fire and those ASTER fire counts where MODIS is likely to classify the data as fire. For example, the number of ASTER fire counts between the 25% and 75% percent probability measure is 4.6 and 3.1 for the version 4 standard and mixed-effects models, respectively, while for the version 3 data, the difference in ASTER fire counts between these same two probabilities is 6.2.

Moving on to models which consider both the number of ASTER fire counts as well as the measure of fire contiguity as relayed through Moran's *I* statistic, the data shown in figure 7 are now shown on figure 10 over a grey-scale image representing the estimated probabilities from model 2, using the standard fixed effects model and data from the MODIS version 4 algorithm. The fitted parameters are given in table 2.

By including the value of Moran's *I*, we see that even for a very small number of ASTER fire counts, when Moran's *I* values are high (i.e the fires are contiguous), there is a high likelihood that MODIS will classify the pixel as 'fire'. The parameters from the random effect version of model 2 are listed in table 2 and shown in figure 11.

Parameters for model 2 applied to the version 3 algorithm are also given in table 2. These models and the results from the modelling on version 4 data, along with the data points, are shown in figure 12. Again, as in the one-dimensional case, model 2 indicates that the version 4 algorithm is more sensitive with respect to ASTER fire counts and Moran's *I*.

For all models, the β_i parameters were statistically significant, with associated '*p*-values' less than 0.001, and variograms of the residuals showed no spatial
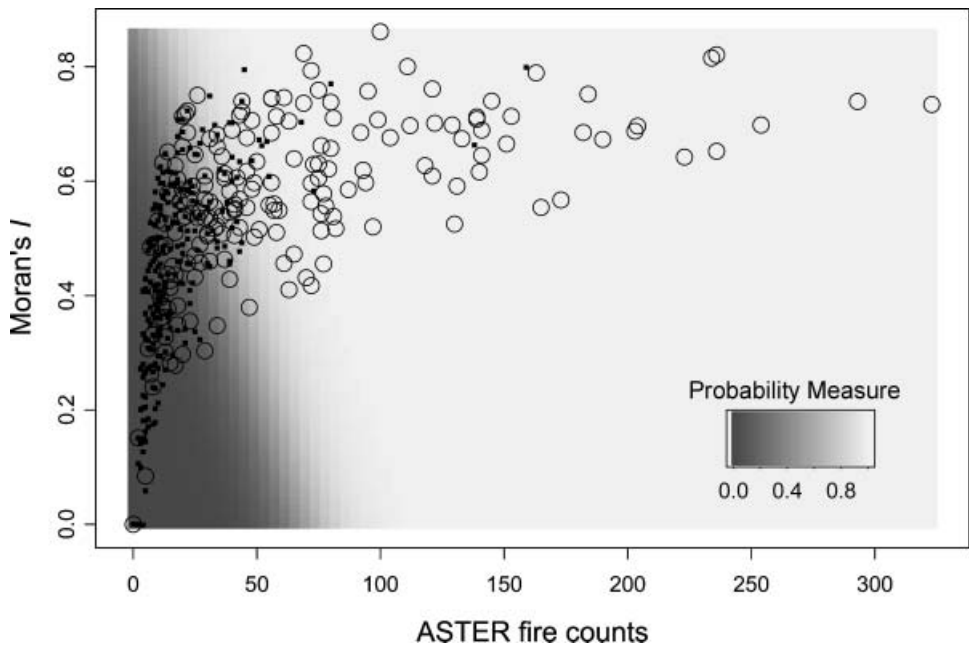
Figure 11.   Estimated probabilities from model 2 with random effects, using the MODIS version 4 algorithm.

autocorrlation within a scene. The residuals are plotted by scene to graphically explore the need for the random-effects model. Figure 13 shows a plot of 'deviance' residuals (Insightful 1999) broken down by scene. A large deviance residual corresponds to an observation that does not fit the model well in the same sense that a large residual for a linear regression model does not fit well (Insightful 1999). For logistic regression modelling in general, the residuals should be centred on zero and show no systematic difference between scenes. The top row of figure 13 shows that some scenes tend to have positive residuals, while some scenes tend to have negative residuals, thus indicating that the 'scene effects' are incorporated in the residuals (Pinheiro and Bates 2000). By accounting for differences between the scenes through the random effects modelling, we see that the residuals behave more appropriately, as seen in the bottom row of figure 13, thus indicating the random effects model as the more appropriate model for this data set. The random-effects models also result in a lower overall residual deviance for both model 1 and 2, for version 4 data and model 2 for version 3 data.

   Figure 14 provides an example of the improved detection capability of version 4 of the MODIS fire-detection algorithm. The images show a fire front moving along a dry, grassy 'dambo' riverbed in Zambia. The fire is along the border between two adjacent MODIS footprints, and thus the relative contribution to either is small. The total number of ASTER fires was 23, and Moran's *I* value was 0.585 (because of the overlapping MODIS footprint on the ASTER fire masks—and because there are no other fires in the two MODIS pixels—the ASTER summary numbers are the same for both MODIS pixels). Using the fitted random-effects models for this case, the probability of detection for version 3 is ~0.18. Indeed, version 3 (figure 14(*a*)) did not detect this fire. Version 4 (figure 14(*b*)), however, with an estimated
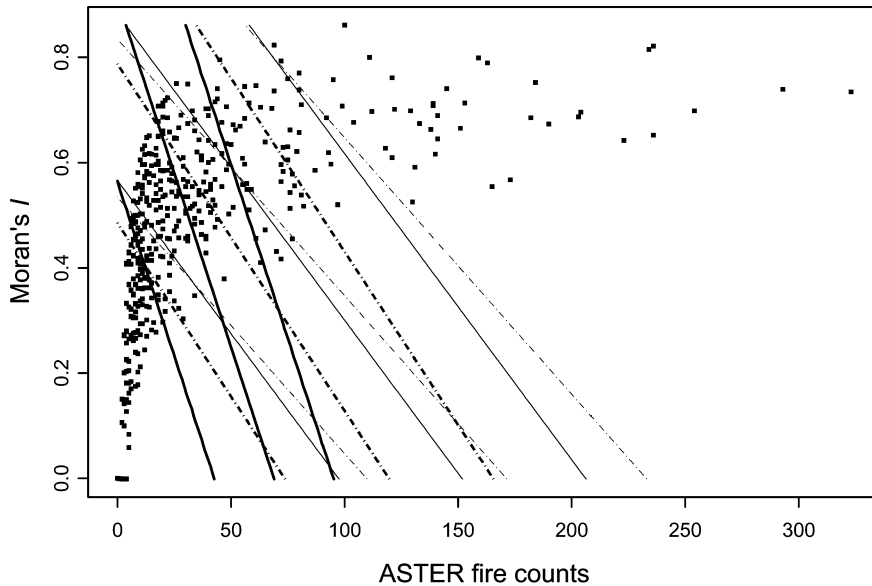
Legend:

The four models are represented as:

——————— Solid bold line: random effects model, MODIS version 4

— · — · — · Dashed bold line: fixed effects model, MODIS version 4

——————— Solid thinner line: random effects model, MODIS version 3

—·—·—·—· Dashed thinner line: fixed effects model, MODIS version 3

Three lines are shown for each model representing, from left to right, the modeled probability at 0.05, 0.50, and 0.95.

Figure 12. Results from model 2 for version 3 and 4 algorithms and fixed and random effects models.

probability of detection of ~0.46, classifies both MODIS pixels covering the fire front as fire.

The analysis thus far has been based on all MODIS pixels covering the ASTER scenes, including areas with no fire activity. Now, we present results focusing on omission errors by removing points where *both* the MODIS classification and ASTER fire counts are equal to zero (referred to as 'zero-points'). Comparing these results to the previous provides an opportunity to assess the influence of the large number of zero-points. Results are given in table 2 and figures 15–17. The new model runs yielded the same general relationship, and the associated parameters were all significant with p-values $<.001$. However, the specific parameter values are different. Comparison of model 1 results (figure 8 vs. figure 15, and figure 9 vs. figure 16) shows less steep curves for the new models, suggesting that the numerous zero-point cases forced the original models to reach low detection probabilities for higher ASTER fire count values; and, because of the symmetric nature of the model function (Agresti 1990), to reach high detection probabilities for lower ASTER fire
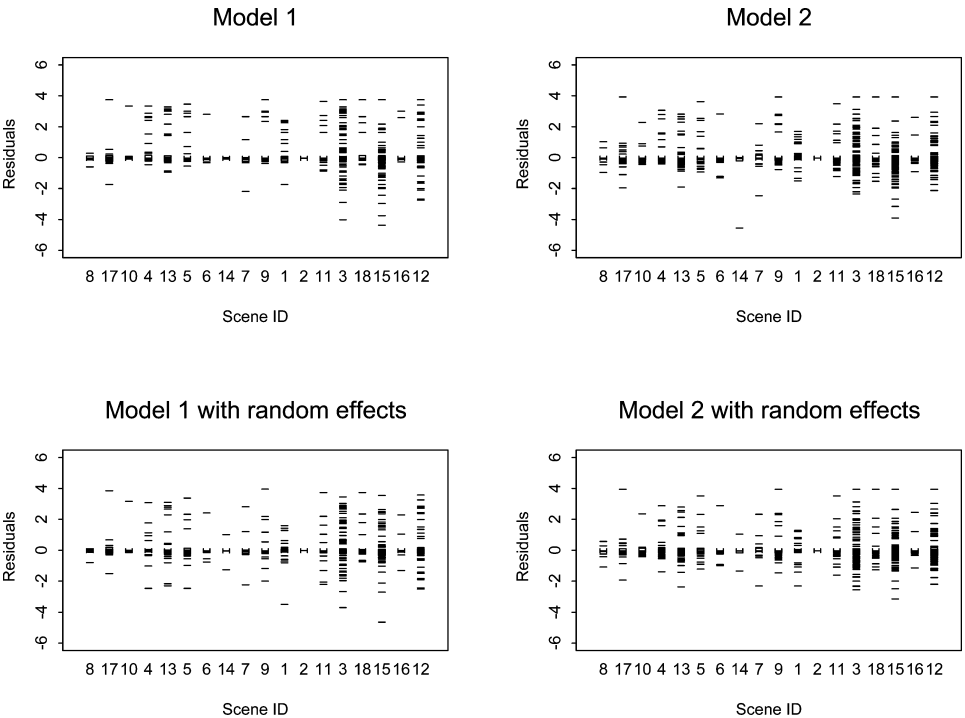
Model 1

Model 2

Model 1 with random effects

Model 2 with random effects

Figure 13. Residual plots for the fixed effects (top row) and random effects (bottom row) for models 1 (left column) and Model 2 (right column).

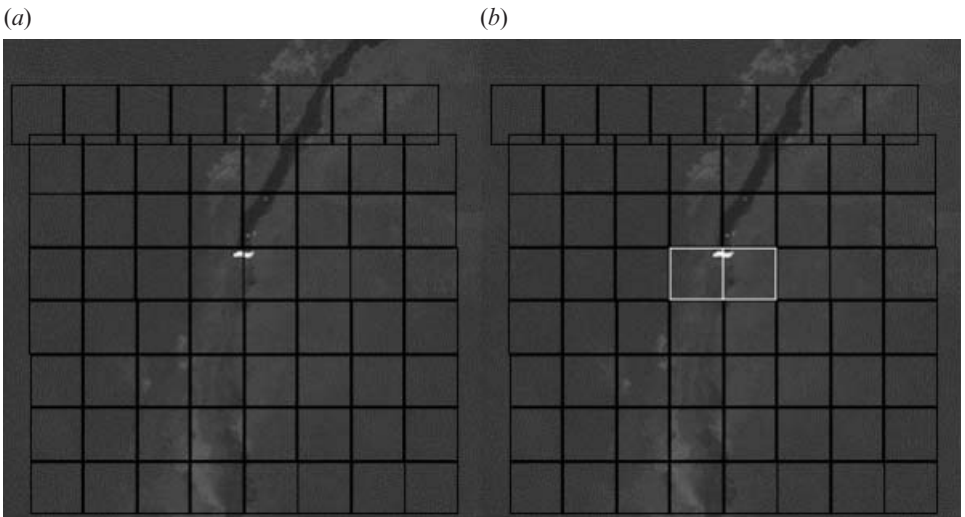(*a*)   (*b*)

Figure 14. Heat signature from fire front working its way along a dry, grassy ('dambo') riverbed in Western Zambia in an ASTER band 9 image from 12 August 2001, centred at 16.6° S 24.4° E. The nominal 1 km MODIS pixel edges are indicated by the black grid lines. Fire pixels detected by the MODIS algorithm are outlined in white.
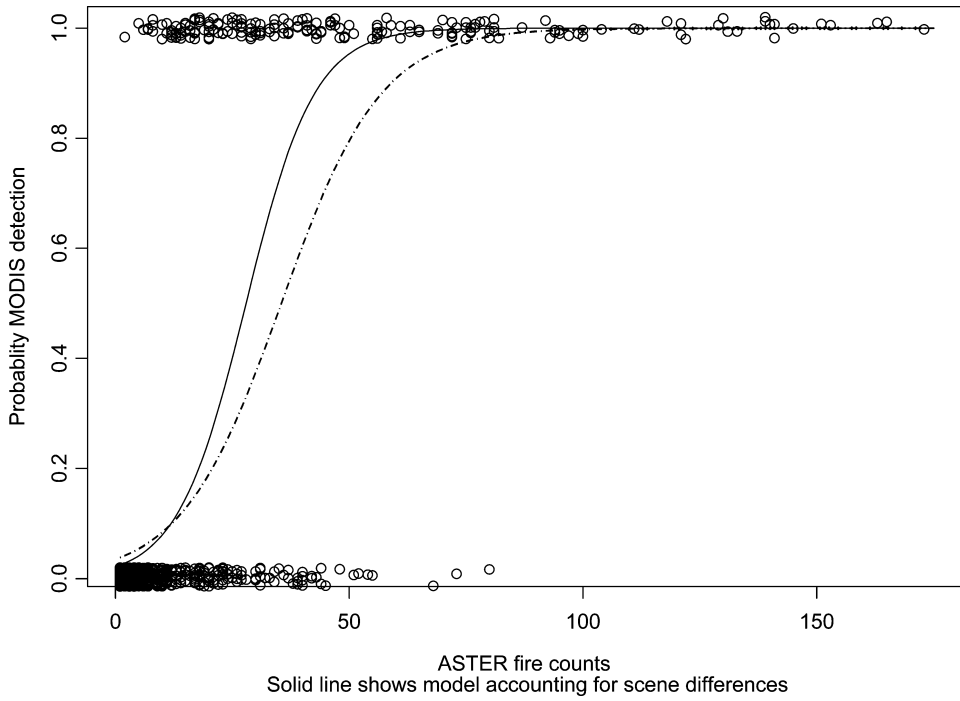
Figure 15. Estimated probabilities from model 1, using the MODIS version 4 algorithm excluding points where both MODIS classification and ASTER counts=0.
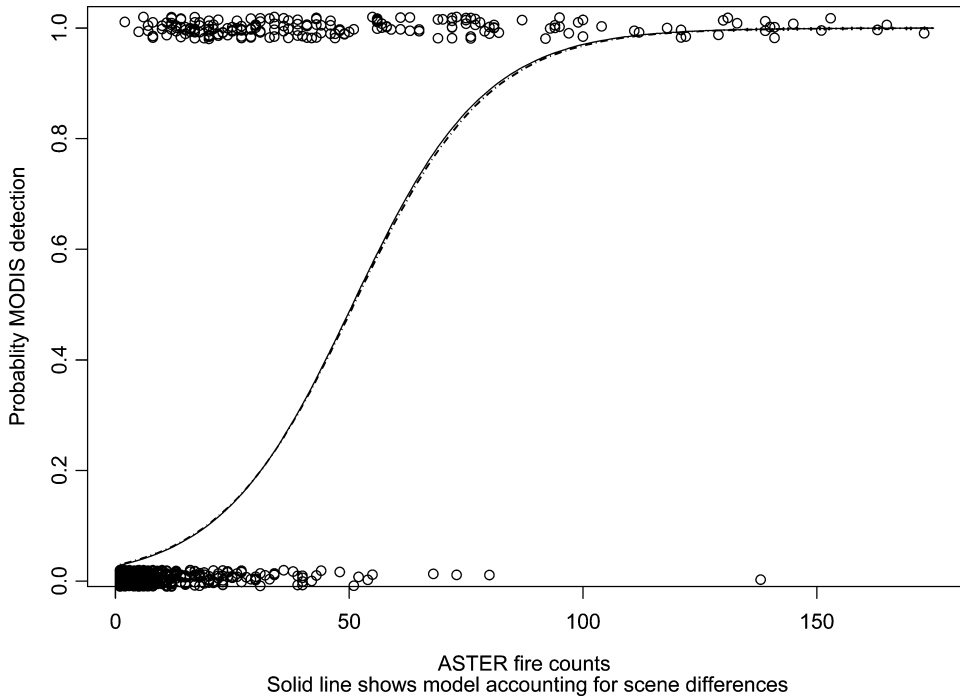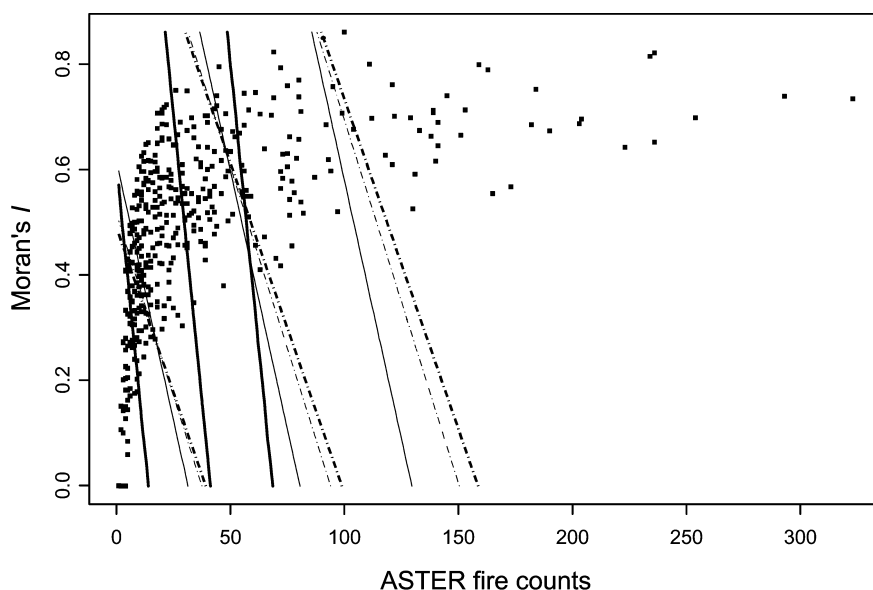

Figure 16. Estimated probabilities from model 1, using the MODIS version 3 algorithm excluding points where both MODIS classification and ASTER counts=0.

Legend:

The four models are represented as:

——————— Solid bold line: random effects model, MODIS version 4

— · — · — · Dashed bold line: fixed effects model, MODIS version 4

——————— Solid thinner line: random effects model, MODIS version 3

–·–·–·–·– Dashed thinner line: fixed effects model, MODIS version 3

Three lines are shown for each model representing, from left to right, the modeled probability at 0.05, 0.50, and 0.95.

Figure 17. Results from model 1 and model 2 for version 3 and 4 algorithms and fixed- and random-effects models, using only data points where ASTER fire counts were greater than zero.

counts. This effect appears to have counteracted the effect of the (ASTER count=0; and MODIS fire='yes') cases (i.e. false MODIS alarms) that were also included in the original analysis. When all the data are included, the large number of zero-points overshadow the few false-alarm pixels.

The more 'stretched out' nature of the ASTER count–detection probability dependence for the new models is also visible in the plots showing the model 2 results (figure 13 vs. figure 17). This comparison also shows less dependence of the detection probability on Moran's *I* for the new models. This is probably due to the fact that the numerous zero-point cases leverage the contour lines towards (negative) 45°.

5. Conclusion/discussion

The questions listed at the start of section 3.3 can be addressed by considering the three lines shown on figures 13 and 17. The three lines given for each model divide

the two-dimensional space of ASTER fire counts and Moran's I into areas corresponding to the three questions. The space to left of the $\pi(x_i)=0.05$ line corresponds to the first question; the space to the right of the $\pi(x_i)=0.95$ line corresponds to the third question; and the space between these two corresponds to the second question.

The modelling done in any statistical analysis involves a choice of which model to use. Resulting parameters and diagnostics are used to assess that choice, but some subjective decision is still involved. That is why here we have presented both the fixed-effects and random-effects models as well as data with and without points where both the MODIS classification and ASTER fire counts were equal to zero. We believe that the random-effects model, by accounting for the variability between ASTER scenes, provided the proper framework to describe these data and is the most relevant to the typical user interested in the MODIS fire product's behaviour over Southern Africa. Providing separate models that include and exclude points where ASTER fire counts are equal to zero provides the user with an envelope between models with the most liberal use of the data (the model including zero-points) and the most conservative (the model that disregards those points). Regardless of the mathematical formulation of the logistic regression model or if the analysis includes the zero-points, it is clear that version 4 of the MODIS fire-detection algorithm has a superior performance to version 3. Separate logistic regression analysis for omission and commission errors might be helpful for further algorithm development; building on the type of analysis started in section 4. To analyse omission errors, only MODIS pixels including ASTER fire pixels should be considered. Similarly, commission errors should be characterized by considering only MODIS pixels with no ASTER fires. In this latter case, however, it may be necessary to include additional or alternative variables in the modelling. Such variables could include distance from the nearest fire pixel, the background temperature, etc. These could extend model 2 of this paper to a more complete multi-dimensional model of detection probabilities as well as a more spatial, cartographic assessment of the errors (Wang and Howarth 1993).

In this paper, we used ASTER band 9 data to derive high-resolution fire maps to serve as an independent measurement to analyse the characteristics and assess the accuracy of the MODIS active fire product. We have taken advantage of the improvement in spatial resolution of the ASTER imagery. However, the ASTER fire maps themselves need to be further developed and their accuracy quantified for proper and correct use as a validation reference. In addition, future processing of many more ASTER scenes will require a more sophisticated and automated multi-spectral ASTER fire-detection procedure. Likewise, the focus has been only ASTER data from Southern Africa. A similar analysis, done with globally distributed ASTER scenes, can address the global validation of the MODIS fire product.

Having ground and/or airborne data available to ascertain additional fire characteristics would enhance the validation process. The analysis presented here is limited to the visual and spectral interpretation of ASTER data. It is a statistical method to provide information on the fire-detection capabilities of MODIS as a function of several basic fire characteristics derived from ASTER. Future work should look to couple ASTER data with field and airborne data to consider such factors as the fine-scale spatial/temporal attributes of the fire radiance signal, various land cover/fire types (e.g. savannah, crop, slash-and-burn forestry), and fire

duration and temporal intensity. An analysis of fire characteristics, coupled with information on detection capabilities from the current or similar studies, would help in deriving regional statistics on the detectable percentage of fires.

Within the framework of the Global Observation of Forest/Land Cover Dynamics (GOFC/GOLD), the fire implementation team is focusing on using regional networks and partners to help test and validate satellite-based fire detection products within their region (Morisette *et al.* 2001). These networks and partnerships can supplement the provision of local expertise and data to help establish the accuracy and reliability of both the ASTER and MODIS fire products. The Southern Africa Fire Network (SAFNET) is currently assisting in assessing the accuracy of the MODIS fire products for this region and their utility for national-scale fire management. Similar activities have been started in Eastern Russia. Involving regional scientists in product validation will help develop a user community, which understands first hand the capabilities and limitations of a given product.

Within a joint LBA (Large-Scale Biosphere–Atmoshere Experiment in the Amazon) Phase II project between IBAMA (Instituto Brasileiro do Meio Ambiente e dos Recursos Naturais Renováveis), NASA and the University of Maryland, validation campaigns are under way in Brazil using airborne high-resolution imagery and ground measurements to characterize ASTER fire-mapping capabilities. The added value of data acquired using 'low-2' SWIR gain, which saturate at much higher radiances, will also be studied. This might allow analysis of fire temperatures from ASTER and their influence on the MODIS fire product.

The validation methods presented in this paper should be applicable to any coincident (or near-coincident) high- and medium-resolution fire observations. This study focuses exclusively on the fire product derived from the MODIS/Terra sensor. Unfortunately, as there is no ASTER instrument on the Aqua platform, the direct validation of MODIS fire products as presented in this paper is not possible for MODIS-derived fire products from the Aqua satellite.

The research presented in this paper reflects the current emphasis that NASA and the MODIS Science Team are placing on product validation (Morisette *et al.* 2002). MODIS has developed a number of improved and new global products (Justice *et al.* 2002b). To quantify the improvement over heritage products and to guide the user community on appropriate use, it is critical to determine the accuracy of the MODIS products. The differences between results for the version 3 and version 4 algorithm show the necessity for validation efforts coinciding with the modification of product algorithms.

With the number of moderate resolution systems currently in orbit and planned for the next decade generating geophysical products, it is a requisite for data producers to include statements concerning the accuracy of their products (Townshend and Justice 2002). However, the methods and protocols for generating and reporting product accuracy is an area for research and development. To help develop the standards and protocols for product validation, a joint international initiative of the Committee on Earth Observations Satellites (CEOS) Land Product Validation Working Subgroup and the GOFC/GOLD programmes has been established on satellite-product validation (Justice *et al.* 2000). We hope this paper can contribute to the continued development of a quantitative protocol for fire-product validation by providing a statistical modelling approach for comparing multiple-resolution fire products.

Acknowledgements

References

AGRESTI, A., 1990, *Categorical Data Analysis* (New York: Wiley).

ARINO, O. and ROSAZ, J.-M., 1999, 1997 and 1998 world ATSR fire atlas using ERS-2 ATSR-2 data. In *Proceedings of the Joint Fire Science Conference, Boise, Idaho, Volume 1*, L.F. Neuenschwander, K.C. Ryan and G.E. Gollberg (Eds), pp. 177–182 (Boise, ID: University of Idaho and the International Association of Wildland Fire).

ARONOFF, S., 1982a, Classfication accuracy: a user approach. *Photogrammetric Engineering and Remote Sensing*, **48**, pp. 1299–1307.

ARONOFF, S., 1982b, The Map Accuracy Report: a user's view. *Photogrammetric Engineering and Remote Sensing*, **48**, pp. 1309–1312.

CONGALTON, R.G. and GREEN, K., 1999, *Assessing the Accuracy of Remotely Sensed Data: Principles and Practices* (Boca Raton, FL: Lewis).

ELVIDGE, C.D. and BAUGH, K.E., 1996, Survey of fires in Southeast Asia and India during 1987. In *Biomass Burning and Global Change: Remote Sensing, Modeling and Inventory Development, and Biomass Burning in Africa, Volume 2*, J.S. Levine (Ed.), pp. 663–670 (Cambridge: MIT Press).

GIGLIO, L., DESCLOITRES, J., JUSTICE, C.O. and KAUFMAN, Y., 2003, An enhanced contextual fire detection algorithm for MODIS. *Remote Sensing of Environment*, **87**, pp. 273–282.

GIGLIO, L., KENDALL, J.D. and TUCKER, C.J., 2000, Remote sensing of fires with the TRMM VIRS. *International Journal of Remote Sensing*, **21**, pp. 203–207.

HAINING, R., 1990, *Spatial Data Analysis in the Social and Environmental Sciences* (Cambridge: Cambridge University Press).

INSIGHTFUL, 1999, *S-Plus 2000 Guide to Statistics, Volume 1* (Seattle, WA: Mathsoft).

JUSTICE, C.O. *et al.* Developments in the validation of satellite products for the study of the land surface. *International Journal of Remote Sensing*, **21**, pp. 3383–3390.

JUSTICE, C.O., GIGLIO, L., KORONTZI, S., OWENS, J., MORISETTE, J.T., ROY, D., DESCLOITRES, J., ALLEAUME, S., PETITCOLIN, F. and KAUFMAN, Y., 2002a, The MODIS fire products. *Remote Sensing of Environment*, **83**, pp. 244–262.

JUSTICE, C.O., KENDALL, J.D., DOWTY, P.R. and SCHOLES, R.J., 1996, Satellite remote sensing of fires during the SAFARI campaign using NOAA advanced very high resolution radiometer data. *Journal of Geophysical Research*, **101**, pp. 23851–23864.

JUSTICE, C.O. and KORONTZI, S.A., 2001, A review of satellite fire monitoring and the requirements for global environmental change research. In F. Ahern, G. Goldammer and C.O. Justice (Eds). *Global and Regional Vegetation Fire Monitoring From Space: Planning a Coordinated International Effort*, pp. 1–18 (The Hague: SPB Academic).

JUSTICE, C.O., TOWNSHEND, J.R.G., VERMOTE, E., MASUOKA, E., WOLFE, R., SALEOUS, N., ROY, D. and MORISETTE, J., 2002b, An overview of MODIS Land data processing and product status. *Remote Sensing of Environment*, **83**, pp. 3–15.

KAUFMAN, Y.J., JUSTICE, C.O., FLYNN, L., KENDALL, J.D., PRINS, E.M., GIGLIO, L., WARD, D.E., MENZEL, W.P. and SETZER, A.W., 1998, Potential global fire monitoring from EOS-MODIS. *Journal of Geophysical Research*, **103**, pp. 32215–32238.

MENZEL, W.P. and PRINS, E.M., 1996, Monitoring biomass burning with the new generation of geostationary satellites. In *Biomass Burning and Global Change: Remote Sensing,*

Modeling and Inventory Development, and Biomass Burning in Africa, Volume 1, J.S. Levine (Ed.), pp. 56–64 (Cambridge, MA: MIT Press).

MORISETTE, J., JUSTICE, C., PEREIRA, J., GRÉGOIRE, J.M. and FROST, P., 2001, 'Report from the GOFC—Fire: Satellite Product Validation Workshop'. *EOS Earth Observer*, September/October, **13**, pp. 15–18.

MORISETTE, J.T. and KHORRAM, S., 2000, Accuracy assessment curves for satellite-based change detection. *Photogrammetric Engineering and Remote Sensing*, **66**, pp. 875–880.

MORISETTE, J.T., PRIVETTE, J.L. and JUSTICE, C.O., 2002, A framework for the validation of MODIS land products. *Remote Sensing of Environment*, **83**, pp. 77–96.

MORISETTE, J.T., GIGLIO, L., CSISZAR, I. and JUSTICE, C.O., 2003, SAFARI 2000 ASTER and MODIS fire data comparison, dry season, 2001. Available on-line at: http://www.daac.ornl.gov from Oak Ridge National Laboratory Distributed Active Archive Center, Oak Ridge, Tennessee, U.S.A.

PINHEIRO, J.C. and BATES, D.M., 2000, *Mixed-Effects Models in S and S-PLUS* (New York: Springer).

PRINS, E.M. and MENZEL, W.P., 1992, Geostationary satellite detection of biomass burning in South America. *International Journal of Remote Sensing*, **13**, pp. 2783–2799.

SWAP, B., PRIVETTE, J., KING, M., STARR, D., SUTTLES, T., ANNEGARN, H., SCHOLES, M. and JUSTICE, C.O., 1998, SAFARI 2000: a southern African regional science initiative. *EOS Earth Observer*, **10**, pp. 25–28.

TAPPIN, L., 1994, Analyzing data relating to the Challenger disaster. *Mathematics Teacher*, **87**, pp. 423–426.

TOWNSHEND, J.R.G. and JUSTICE, C.O., 2002, Towards operational monitoring of terrestrial systems by moderate-resolution remote sensing. *Remote Sensing of Environment*, **83**, pp. 351–359.

WANG, M. and HOWARTH, P., 1993, Modeling errors in remote sensing image classification. *Remote Sensing of Environment*, **45**, pp. 261–271.

WOLFE, R.E., NISHIHAMA, M., FLEIG, A.J., KUYPER, J.A., ROY, D.P., STOREY, J.C. and PATT, F.S., 2002, Achieving sub-pixel geolocation accuracy in support of MODIS land science. *Remote Sensing of Environment*, **83**, pp. 31–49.

YAMAGUCHI, Y., KAHLE, A.B., TSU, H., KAWAKAMI, T. and PNIEL, M., 1998, Overview of Advanced Spaceborne Thermal Emission and Reflection Radiometer (ASTER). *IEEE Transactions on Geoscience and Remote Sensing*, **46**, pp. 1062–1071.